Aggregation of carboxyl-modified polystyrene nanoplastics in water with aluminum chloride: Structural characterization and theoretical calculation

Yanyan Gong[a, #]*, Yang Bai[a, #], Dongye Zhao[b], Qilin Wang[c]

[a] *Guangdong Key Laboratory of Environmental Pollution and Health, School of Environment, Jinan University, Guangzhou 511443, China*

[b] *Environmental Engineering Program, Department of Civil & Environmental Engineering, Auburn University, Auburn AL 36849, USA*

[c] *Center for Technology in Water and Wastewater, School of Civil and Environmental Engineering, University of Technology Sydney, Sydney, NSW, 2007, Australia*

[#]*Equal contributions*

*Corresponding author. E-mail address: yanyangong@jnu.edu.cn (Y. Gong).

Abstract: Nanoplastics (NPs) pollution of aquatic systems is becoming an emerging environmental issue due to their stable structure, high mobility, and easy interactions with ambient contaminants. Effective removal technologies are urgently needed to mitigate their toxic effects. In this study, we systematically investigated the removal effectiveness and mechanisms of a commonly detected nanoplastics, carboxyl-modified polystyrene (PS-COOH) via coagulation and sedimentation processes using aluminum chloride ($AlCl_3$) as a coagulant. PS-COOH appeared as clearly defined and discrete spherical nanoparticles in water with a hydrodynamic diameter of 50 nm. The addition of 10 mg/L $AlCl_3$ compressed

and even destroyed the negatively charged PS-COOH surface layer, decreased the energy barrier, and efficiently removed 96.6% of 50 mg/L PS-COOH. The dominant removal mechanisms included electrostatic adsorption and intermolecular interactions. Increasing the pH from 3.5 to 8.5 sharply enhanced the PS-COOH removal, whereas significant loss was observed at pH 10.0. High temperature (23 ^{o}C) favored the removal of PS-COOH compared to lower temperature (4 ^{o}C). High PS-COOH removal efficiency was observed over the salinity range of 0–35‰. The presence of positively charged Al_2O_3 did not affect the PS-COOH removal, while negatively charged SiO_2 reduced the PS-COOH removal from 96.6% to 93.2%. Moreover, the coagulation and sedimentation process efficiently removed 90.2% of 50 mg/L PS-COOH in real surface water even though it was rich in inorganic ions and total organic carbon. The fast and efficient capture of PS-COOH by $AlCl_3$ via a simple coagulation and sedimentation process provides a new insight for the treatment of NPs from aqueous environment.

Keywords: Nanoplastics; Coagulation; Sedimentation; Aluminum chloride; Removal

1. Introduction

Plastic products are being widely applied in a variety of industries, such as packaging (Ivleva et al., 2017), construction materials (Hernandez et al., 2017), daily personal care products, vehicles, clothing, and electronics (Song et al., 2017) due to their excellent physicochemical properties of ease of production, durability, light weight, and low cost (Saliu et al., 2018). The major routes of plastics to the environment concern wastewaters and urban runoffs (Besseling et al., 2017; Carr et al., 2016). After entering into water bodies, some larger-size plastics fragmentize into smaller nanoplastics (NPs) with sizes ranging from 1 to 100 nm through weathering, biodegradation (Andrady, 2011), photodegradation, thermal degradation (da Costa et al., 2016), and the movement of water flow (Auta et al., 2017). While the concentrations of NPs in natural water bodies are estimated to be lower than 1 mg/L (Lenz et al., 2016), NPs have become a growing environmental concern since they can be easily swallowed and ingested by organisms and accumulated along the food chain (Chae and An, 2017; Yang et al., 2015). Moreover, due to their hydrophobicity and large surface-to-volume ratio, NPs often show high adsorption capacities for an array of toxic chemicals such as persistent organic pollutants (e.g., polychlorinated biphenyls, organochlorine pesticides, polycyclic aromatic hydrocarbon, dichlorodiphenyltrichloroethane) and heavy metals (e.g., Zn, Pb, and Cu) (do Sul and Costa, 2014), and thus play important roles in the fate and transport of the pollutants in the environment. The adsorbed pollutants on NPs can then desorb and affect the metabolic and physiological processes as well as human and ecological health. Thus, efficient and feasible approaches for removal of NPs from natural water bodies are urgently needed.

Several advanced treatment technologies have been proposed and employed for removing microplastics (MPs), including membrane bio-reactor, rapid sand filtration, and dissolved air flotation (Talvitie et al., 2017). However, these technologies bear with some

serious drawbacks, such as inefficiency due to the degradation-resistance of plastics, the large occupation of space, and potential point pollution source of microplastics and NPs (Carr et al., 2016; Lu et al., 2018). More importantly, these methods were designed for the removal of MPs and were less effective for the removal of NPs due to the smaller particle size (da Costa et al., 2016). Coagulation has attracted particular attention due to its low-cost and high removal performance (You et al., 2019). Various inorganic coagulants such as polyaluminum chloride, aluminum-based salts, and iron-based salts (He et al., 2019) have been extensively applied in the process of coagulation. The simple introduction of these inorganic coagulants can compress the electric double layer and settle unstable particles in water by forming larger flocs (Ma et al., 2019). For example, Skaf et al. (2020) found that coagulation using alum at 5 and 10 mg/L reduced the turbidity of 5 mg/L microspheres (1-5 μm diameter) from initial 16 NTU to less than 1.0 NTU. Zhou et al. (2021) reported that 90 mg/L of the polyaluminium chloride (PAC) was able to remove 77.8% and 29.7% of 500 mg/L polystyrene and polyethylene with sizes smaller than 5 mm, respectively. Charge neutralization occurred in the coagulation of both PS and PE and agglomeration adsorption was observed in the PS system. The hydrolysis products of coagulants played a predominant role rather than the hydrolysis process. Although NPs may share some of the properties of MPs, their size-dependent properties distinguish them from MPs with respect to the transport properties and interactions with natural colloids (Gigault et al., 2021). Yet, to the best of our knowledge, few studies have been reported about the remediation of NPs-contaminated water by coagulation. The removal effectiveness and underlying mechanisms are not clear. Moreover, as complex water chemistry conditions such as pH (Liu et al., 2018), temperature (Qiu et al., 2019), salinity (Wu et al., 2019), and inorganic colloids (Oriekhova and Stoll 2018) are known to affect the aggregation of NPs, the influences and affecting mechanisms of these factors on NPs removal by coagulation have not yet been systematically investigated.

To fill in the abovementioned knowledge gaps, the overall goal of this study was to determine the governing removal mechanisms of NPs in natural waters by coagulation and sedimentation and explore the effects of environmental chemistry. Carboxyl-modified polystyrene (PS-COOH) is one of the most commonly detected plastics in the environment (Casado et al., 2013) and was applied as representative NPs in this study. The specific objectives were to: (1) compare the removal efficiencies of PS-COOH via commonly used coagulants at various dosages; (2) examine the effects of pH, temperature, salinity, and inorganic colloids on the removal effectiveness; (3) study the removal of PS-COOH in real surface waters; and (4) explore the underlying mechanisms affecting NPs aggregation via theoretical calculation and physical characterizations.

2. Materials and methods

2.1. Materials

All chemicals used in this study were in analytical grade or higher. PS-COOH NPs (density of 1.05 g/cm^3 and refractive index of 1.59) with hydrodynamic diameters of 50 nm were obtained from Huge Biotechnology (Shanghai, China). According to the manufacturer, there are small amounts of surfactants in the stock solution and the concentration of PS-COOH in the stock solution is 50 g/L as PS-COOH or 49.6 g/L as total organic carbon (TOC). The PS-COOH NPs stock solution was diluted in deionized water to achieve the desired target concentrations. Aluminum chloride hexahydrate ($AlCl_3 \cdot 6H_2O$), sodium hydroxide (NaOH), and ferric chloride hexahydrate ($FeCl_3 \cdot 6H_2O$) were purchased from Macklin Biochemical Technology (Shanghai, China). Polyaluminum chloride (PACl) was obtained from Damao Chemical Reagent Technology (Tianjin, China). Sodium chloride (NaCl) was obtained from Jinhuada Chemical Reagent Technology (Guangzhou, China). Silicon dioxide (SiO_2) with a particle size of 50 nm was purchased from Shunping

Biochemical Technology (Guangzhou, China). Alumina (Al_2O_3) with a particle size of 20 nm was purchased from Aladdin industrial corporation (Shanghai, China). As a proxy for inorganic colloids, suspensions of SiO_2 and Al_2O_3 (500 mg/L) were prepared in ultrapure water and sonicated for 15 min with a CNC ultrasonic cleaner (KQ-500DE, Kunshan, China), respectively. All samples in this study were prepared using deionized water unless stated otherwise.

2.2. Characterization of PS-COOH NPs

The morphology of PS-COOH before and after reaction was visuarized by scanning electron microscopy (SEM) (Supra55, Zeiss, Jena, Germany). The average hydrodynamic diameters and zeta potentials (ζ) were characterized using a Malvern Zetasizer Nano ZS instrument (Nano ZSE, Malvern Instruments, Worcestershire, U.K.). The polydispersivity index (PDI) value was derived according to the size distributions of PS-COOH:

$$PDI=\sigma^2/Z_D^2 \quad (1)$$

where σ is the standard deviation and Z_D is the average hydrodynamic diameter. The surface functional groups of PS-COOH NPs before and after reaction were analyzed by fourier transform infrared spectroscopy (FTIR, Nicolet iS5, Thermo Fisher Scientific, Waltham, MA, U.S.A.). The collected flocs were vacuum-dried in a freeze drier (SCIENTZ-10N, Ningbo, China) at -40 ^{o}C for FTIR analysis.

2.3. Coagulation and precipitation experiments

Standard jar tests for testing the removal effectiveness of PS-COOH NPs from water were carried out via coagulation, flocculation, and sedimentation. Jar testers (Meiyu, MY3000-6B, Wuhan, China) consisting of six paddle stirrers, jars, and 500 mL glass beakers were applied. Each beaker was loaded with 300 mL of PS-COOH NPs suspension with an

initial concentration of 50 mg/L and an initial pH of 6.5±0.1. Batch experiments were carried out following previously reported mixing and settling procedures (Qiu et al., 2019): Sequential mixing at 70 rpm for 1 min, 180 rpm for 30 s, 40 rpm for 15 min, 30 rpm for 15 min, 20 rpm for 15 min, and final 15 rpm for 25 min, and then settling for 30 min under gravity. A small amount of the mixture after 1 min mixing at 70 rpm was taken immediately for time-resolved DLS measurement to monitor the change of average hydrodynamic diameters of PS-COOH as a function of time. The size of PS-COOH was recorded every 20 s and lasted for 10 min, with the first record at 20 s after the beginning of the DLS measurement. At the end of settling, 20 mL of the supernatant was sampled submerged at 1/3 depth of the liquid surface for residual turbidity and PS-COOH NPs concentration analysis. The NPs removal efficiency was calculated based on the differences between the initial and final concentrations of aqueous PS-COOH NPs.

To determine the effects of alternative coagulants and coagulant dosage, the jar tests were conducted with various concentrations of $AlCl_3$, $FeCl_3$, and PACl (2.5, 5, 10, 20, and 40 mg/L, respectively. For all the following experiments, the initial concentrations of PS-COOH and $AlCl_3$ were set at 50 mg/L and 10 mg/L, respectively. To explore the effects of pH, the initial pH of the mixture of was adjusted to 3.0, 4.5, 6.5, 8.5, and 10.0 with NaOH or HCl solutions, and the final pH was recorded in respective figure captions. To investigate the effects of reaction temperature, the temperature was set at 4 and 23 ^{o}C, which represent the average temperature of seawater in winter and room temperature, respectively. The low temperature was maintained by placing the beaker in cold ice-water bath with ice bags. To study the effects of salinity, known amounts of NaCl were dissolved into the suspensions to obtain various salinities ranging from 5‰ to 35‰ to simulate real environmental conditions in a representative estuary (Wu et al., 2019). To probe the effects of inorganic colloids, 30 mg/L of Al_2O_3 and 50 mg/L of SiO_2 were mixed with 50 mg/L of PS-COOH suspension,

166 respectively, before reaction. All experiments were conducted in duplicate and the average
167 results were reported with errors indicating the standard deviations.
168
169 *2.4. Removal of PS-COOH in real surface water*
170 Surface water samples were collected from the top 5 cm of the water column from
171 Xinzao Town, Panyu District, Guangzhou, China. The latitude/longitude of the sampling site
172 was 113.41/23.03. The collected sample was first filtrated through a 0.45 μm membrane
173 filter (mixed cellulose esters) to remove suspended solids. To facilitate the following PS-
174 COOH removal experiments, the surface water was pre-spiked with PS-COOH solution to
175 obtain a PS-COOH concentration of 50 mg/L. Coagulation and precipitation experiments
176 were then conducted following the same manner as described in section 2.3. Control tests
177 were performed in the absence of $AlCl_3$ under otherwise identical conditions.
178
179 *2.5. Interaction energy calculation by DLVO theory*
180 The Derjaguine-Landaue-Verweye-Overbeek (DLVO) theory states that particles are
181 subject to van der Waals interaction forces and electrostatic repulsion forces and is widely
182 used to calculate the surface interaction energy of particles as a function of separation
183 distance and to predict the aggregation behavior of particles (Derjaguin and Landau, 1993).
184 The interaction force of the PS-COOH NPs was determined treating the particle-particle as a
185 sphere-sphere geometry. Detailed information on the calculations is provided in the
186 supporting information (**Section S1**).
187
188 *2.6. Analytical methods*
189 pH was measured using a PB-10 pH meter (Sartorius, Gottingen, Germany). The PS-
190 COOH concentration was determined via a total organic carbon analyzer (TOC-LCPH,

Shimadzu Corporation, Japan) with a PS-COOH detection limit of 1.0 mg/L. Turbidity was determined using a Turbidity Meter (TN-100, Shanghai, China) and the detection limit was 0.27 NTU. The concentrations of K, Ca, Na, and Mg in aqueous solutions were determined by an inductively coupled plasma mass spectrometer (ICP-MS, NexION 350X, PerkinElmer, Shelton, CT, U.S.A.), and the detection limits were 4.50, 6.61, 6.36, and 1.94 μg/L, respectively.

3. Results and discussion

3.1. Characterization of PS-COOH

PS-COOH NPs appeared as clearly defined and discrete spherical nanoparticles and were stable and well dispersed in water (**Fig. 1a**). After coagulation, due to the bridges formed between aluminum salt and PS-COOH (Wu et al., 2020), flocs shaped as open structures were observed as presented in **Fig. 1b**. Due to the presence of negatively charged carboxyl functional groups and surfactant, the zeta potential of PS-COOH NPs varied from -27.8±3.5 mV at pH 3 to -49.6±3.6 mV at pH 10 (**Fig. 1c**). PS-COOH NPs demonstrated a relatively uniform size distribution and the mean hydrodynamic diameter was equal to 50±2 nm as shown in the size distribution histograms (**Fig. 1d**). The polydispersivity index value (0.025) for the suspensions of PS-COOH NPs was less than 0.2, which indicated that PS-COOH NPs were stable and well dispersed in water without significant aggregation (Izquierdo et al., 2005).

3.2. Effects of different coagulant and coagulant dosage on the removal of PS-COOH

The removal efficiencies of PS-COOH and the turbidity removal via three commonly used coagulants, namely, $AlCl_3$, $FeCl_3$, and PACl at different dosages ranging from 2.5 to 40 mg/L were compared in **Figs. 2a and b**. The coagulants effectively reduced the PS-COOH in

the aqueous phase. Generally, increasing the coagulant dosage (0–10 mg/L for $AlCl_3$ and $FeCl_3$, 0–5 mg/L for PACl) enhanced the PS-COOH removal. For instance, increasing the $FeCl_3$ dosage from 2.5 to 5 and further to 10 mg/L enhanced the PS-COOH removal efficiency from 8.7% to 89.6% and further to 95.8%. As shown in **Fig. 2c**, after coagulation with 2.5-10 mg/L $FeCl_3$ or $AlCl_3$, the pH values in the systems were in the range of 4.0-5.0, where Fe mainly presented as positively charged $Fe(OH)_2^+$ (Wang et al, 2013) and Al as positive hydrolyzates such as $Al(OH)_2^+$, $Al_2(OH)_2^{4+}$, and $Al_3(OH)_4^{5+}$ (Zhang et al., 2008). The enhancement in the PS-COOH removal was due to the charge neutralization (**Fig. 2d**) and compression of electrostatic double layer (Li et al., 2019). Yet, no advantage was observed at a higher dosage. For instance, further increasing the $FeCl_3$ dosage from 10 to 40 mg/L led to a statistically significant decline in the PS-COOH removal efficiency (4.5%, *p* value = 0.002). Similarly, increasing the PACl dosage from 5 to 40 mg/L led to a statistically significant decline in the PS-COOH removal efficiency (2.8%, *p* value = 0.016). Increasing the $FeCl_3$ dosage from 10 to 40 mg/L significantly decreased the system pH from 4.1 to 3.1 where Fe mainly presented as $Fe(OH)_2^+$ and $Fe(OH)^{2+}$ (Wang et al., 2013). The decline in PS-COOH was due to the charge reversal effect (**Fig. 2d**) leading to the restabilization of the particles. Meanwhile, further increasing the $AlCl_3$ dosage from 10 to 40 mg/L resulted in statistically insignificant changes in the removal efficiency (*p* value = 0.71). It can be seen that the zeta potential of PS-COOH remained constant at -2.9 mV at $AlCl_3$ dosage ranging from 10 to 40 mg/L (**Fig. 2d**).

Correspondingly, the residual turbidity was also compared in **Fig. 2b**. In general, the results concurred with the classical coagulation curve. The initial turbidity of 50 mg/L of PS-COOH NPs was determined to be 4.83 NTU, exceeding the quality standard of 1 NTU in drinking water (GB 5749-2006, China). When the concentration of $AlCl_3$, $FeCl_3$, and PACl increased from 0 to 5, 5, and 2.5 mg/L, the turbidity increased to 18.60, 8.04, and 18.00 NTU,

241 respectively. Further increasing the coagulant dosage to 20.0, 10.0, and 5 mg/L decreased the
242 turbidity to 0.99, 1.09, and 0.68 NTU, respectively. Yet, the turbidity was raised up to 11.60,
243 9.06, and 16.70 NTU, respectively, with a coagulant dosage of 40 mg/L. The increase of the
244 residual turbidity was probably due to (1) the formation of new disturbing particles, e.g.,
245 hydroxides, which are not settled (Rajala et al., 2020), and (2) the formed loose and easily
246 broken flocs with excessive coagulant (Wu et al., 2007).
247 Considering the PS-COOH removal efficiency, the residual turbidity, and the availability
248 of coagulants, 10 mg/L of $AlCl_3$ was selected in the following experiments.
249
250 *3.3. Interactions between PS-COOH and $AlCl_3$*
251 The introduction of inorganic ions can alter the surface charge of nanoparticles,
252 controlling their aggregation behavior (Wong et al., 2012). Our results showed that the zeta
253 potentials of PS-COOH were negative with the addition of 0–40 mg/L $AlCl_3$. The zeta
254 potential became less negative as $AlCl_3$ concentration increased (**Fig. 2d**). The electrostatic
255 interaction between negatively charged PS-COOH and positively charged aluminum ions led
256 to charge neutralization, and obvious aggregation of PS-COOH was observed (**Fig. S1**). The
257 change of hydrodynamic size over time for PS-COOH after mixing with $AlCl_3$ at different
258 concentrations was shown in **Fig. 3a**. The PS-COOH dispersed well in water with a
259 hydrodynamic size of 50 nm. Similarly, the hydrodynamic size remained constant at about
260 50 nm at a $AlCl_3$ concentration of 2.5 mg/L. With an increase of $AlCl_3$ concentration to 5,
261 10, 20, and 40 mg/L, the hydrodynamic size increased readily to 248, 1315, 2462, and 4544
262 nm, respectively after 10 min, and an obvious aggregation of PS-COOH was observed (**Fig.**
263 **S1**).
264 To obtain a better understanding of the stability of PS-COOH at different $AlCl_3$
265 concentrations, the attachment efficiency (α) and aggregation rate (nm/s) of PS-COOH NPs

were determined. When the $AlCl_3$ concentration increased from 2.5 to 40 mg/L, the positively charged aluminum ions can compress and even destroy the stable negatively charged PS-COOH surface layer or electron double layer (Vangara et al., 2017), and the stabilizing Coulomb forces between two particles decreased (Petosa et al., 2010), resulting in higher attachment efficiency. As shown in **Fig. 3b**, the α value increased from 0.001 to 0.319 as $AlCl_3$ concentration increased from 2.5 to 20 mg/L. This stage is known as reaction-limited aggregation regime ($\alpha < 1$) (Lin et al., 2016). In this regime, the increase in $AlCl_3$ elevated the degree of charge screening and led to an increase in aggregation kinetics, as reflected by the rise in the α value. When the concentration of $AlCl_3$ increased to 40 mg/L, the α value reached 1 and this stage is defined as diffusion-limited aggregation regime (Lin et al., 2016), where the aggregation kinetics approached the theoretical maximum. In this regime, the aggregation kinetics was independent on the $AlCl_3$ concentration. The distinct regimes indicated that electrostatic interactions occurred between PS-COOH and $AlCl_3$ (Wang et al., 2020). Correspondingly, the aggregation rate of PS-COOH was enhanced from 0.005 nm/s to 4.163 nm/s with the increase of $AlCl_3$ concentration from 2.5 to 40 mg/L (**Table S1**). The colloidal stability of PS-COOH in the absence and presence of $AlCl_3$ in aqueous phase is supported by the DLVO analysis as shown in **Fig. S2**. In the absence of $AlCl_3$, the energy barrier between PS-COOH was substantially high (29 KT) (**Fig. S2a**), which resulted in the well dispersion of PS-COOH in the solution. The energy barrier decreased to 2.5–4.8 KT and finally dropped below 0 KT with the addition of 2.5 to 40 mg/L $AlCl_3$ (**Fig. S2b**). The interaction between PS-COOH and aluminum ions changed the surface chemistry of PS-COOH and inhibited the negative zeta potential of PS-COOH. Thus, the addition of $AlCl_3$ promoted the homoaggregation of PS-COOH. It is noteworthy that the DLVO interaction energy calculation predicts a repulsive force among PS-COOH in 5 and 10 mg/L of $AlCl_3$ (**Fig. S2b**). However, obvious aggregation of PS-COOH was observed in both

conditions (**Fig. S1**). The discrepancy can be explained by the fact that the introduced aluminum ions adsorbed onto the surface of PS-COOH, rendering the PS-COOH' surface electrostatically heterogeneous (Sennato et al., 2009). Yet, the DLVO interaction energy prediction only uses the mean value of surface charge, which neglects the effects of the heterogeneity on the interacting surfaces (Cai et al., 2018).

To further investigate the possible interaction between $AlCl_3$ and PS-COOH during the coagulation process, the stretching frequencies of $AlCl_3 \cdot 6H_2O$ and PS-COOH before and after coagulation were measured (**Fig. 4** and **Fig. S3).** For $AlCl_3 \cdot 6H_2O$ (**Fig. 4a**), four major peaks were evident, including bound and isolated hydroxyl groups and adsorbed water molecules group at 3356 cm^{-1} (Costa et al., 1999), the bending of water molecules at 1630 cm^{-1} (Costa et al., 1999), and the Al-O group at 595 cm^{-1} and 855 cm^{-1} (Beran et al., 2001). For PS-COOH flocs after interaction with $AlCl_3$ (**Fig. 4b**), the characteristic band at 3400 cm^{-1} was ascribed to the H-O-H vibrations of adsorbed water (Li et al., 2004). The absorption peaks observed at 3091 cm^{-1} and 3023 cm^{-1} were ascribed to the C-H stretching vibrations in benzene rings (Yuan et al., 2019). The peaks appearing at 2926 cm^{-1} and 2849 cm^{-1} corresponded to the asymmetric and symmetric stretching vibrations of C-H. The absorption peak at 1705 cm^{-1} represented the existence of -COOH groups (Hu et al., 2019). The absorption bands located at 1490 cm^{-1} and 1453 cm^{-1} was assigned to the vibration of monosubstituted benzenes (Han et al., 2017). The absorption peaks at 757 cm^{-1} and 701 cm^{-1} were related to the bending vibrations of hydrogen atoms on monosubstituted benzene rings (Ding et al., 2015). These characteristic peaks representing PS-COOH were consistent with previously reported studies (**Fig. S3**) (Chen et al., 2016; Han et al., 2020). After reaction with $AlCl_3$, a new peak at 1600 cm^{-1} representing the COO-Al group (Lee et al., 2000) was observed, which might be due to the formation of bridges between the surface functional groups of PS-COOH and aluminum (Wu et al., 2020). Furthermore, the peak at

550 cm^{-1} and 1072 cm^{-1} corresponded to Al-OH (Djebaili et al., 2015; Perkins and Palmer 2000). The pH of the system after reaction with different concentrations of $AlCl_3$ was shown in **Fig. S3**. As expected, increasing the $AlCl_3$ concentration progressively decreased the pH values due to the OH^- consumption by the $AlCl_3$ hydrolysis. These results suggest that the dominant reaction mechanisms between PS-COOH NPs and $AlCl_3$ include electrostatic adsorption and intermolecular forces.

3.4. Effects of pH on PS-COOH removal

Effects of pH on PS-COOH removal by $AlCl_3$ was investigated over the initial pH range of 3.0–10.0. The PS-COOH removal efficiency increased sharply from 12.0% at pH 3.0 to 96.4% at pH 8.5, and then decreased to 83.7% when pH reached 10.0 (**Fig. 5a**). Solution pH can affect both the surface potential of PS-COOH and speciation of aluminum. The surface of PS-COOH maintained negatively charged (-27.8–(-49.6) mV) (**Fig. 5b**) and the hydrodynamic diameter remained constant at 50 nm (**Fig. 5c**) over the pH range. At pH 3.0, Al mainly presented as hydrated monomer aluminum ($Al(H_2O)_6^{3+}$) (Hu et al., 2006). When pH increased to 4.5, the main species are positive hydrolyzates such as $Al(OH)_2^+$, $Al_2(OH)_2^{4+}$, and $Al_3(OH)_4^{5+}$ (Zhang et al., 2008). When the pH reached 8.5, highly polymeric positive hydrolyzates, such as $[AlO_4Al_{12}(OH)_{24}(H_2O)_{12}]^{7+}$ (Al_{13}), which was reported to be the most effective coagulation species in aluminum-based coagulants due to its strong charge neutralization capability and high structure stability (Bottero et al., 1982; Gregory and Dupont, 2001), was formed. These positive hydrolyzates possessed strong ability of neutralizing the negative charges of PS-COOH and formed flocs with PS-COOH through adsorption and bridging, resulted in the destabilization of nanoplastics. Therefore, as the pH increased from 3.0 to 8.5, the zeta potential of PS-COOH in the presence of $AlCl_3$ changed from -11.7 mV to -3.0 mV (**Fig. 5b**) and the hydrodynamic diameters increased

sharply from 55 to 4755 nm after 10 min (**Fig. 5c**), leading to an improved PS-COOH aggregation rate (from 0 at pH 3.0 to 2.63 nm/s at pH 8.5) (**Table S1**) and an enhanced PS-COOH removal efficiency. When pH reached 10.0, the dominate hydrolyzate was transformed to negatively charged $Al(OH)_4^-$ (Yang et al., 2010). The zeta potential was reduced to -16.3 mV and the corresponding hydrodynamic diameter remained at 67 nm, resulting in an aggregation rate of 0 and a declined PS-COOH removal efficiency of 83.7%. Increasing the pH from 8.5 to 10.0 enhanced the repulsive energy barrier between PS-COOH from <0 to 5.0 KT as shown in **Fig. S4**.

3.5. Effects of temperature on PS-COOH removal

Effects of temperature on PS-COOH removal efficiency by $AlCl_3$ was investigated at pH 6.5. **Fig. 6a** shows that increasing the temperature from 4 to 23 ^oC significantly enhanced the PS-COOH removal efficiency from 92.1% to 96.6% (p value of 0.001 at the 0.05 level of significance).

It is reported that the NPs were more stable at the lower temperature compared to those at the higher temperature (Singh et al., 2019). The hydrodynamic diameters of PS-COOH without the addition of $AlCl_3$ at 4 and 23 ^oC remained constant at 50 nm and the aggregation rates were both 0 (**Table S1**). High temperature increases the solubility of $AlCl_3$, decreases the viscosity of water, enhances the Brownian motion and the molecular collision rate, and increases the reaction rate constant, which is conducive to the formation of larger flocs of PS-COOH (Qiu et al., 2019). As shown in **Fig 6b**, with the addition of $AlCl_3$, when the temperature was increased from 4 ^oC to 23 ^oC, the hydrodynamic diameters of PS-COOH was increased from 800 nm to 1400 nm after 10 min and the aggregation rate of PS-COOH was enhanced from 0.888 to 1.138 nm/s (**Table S1**).

3.6. Effects of salinity on PS-COOH removal

The aggregation kinetics and removal efficiency of PS-COOH with or without the addition of $AlCl_3$ were studied over a range of salinities from 0 to 35‰. In the absence of $AlCl_3$, the zeta potential of PS-COOH changed from -43.6 mV to -36.5 and -34.2 mV, respectively, as the salinity increased from 0 to 5‰ and 10‰, and then more sharply to -25.8 mV as the salinity reached 35‰ (**Fig. 7a**). Accordingly, the hydrodynamic size of PS-COOH with salinities of 5‰ and 10‰ remained constant at 50 nm (**Fig. 7b**) with an aggregation rate of 0 (**Table S1**). Yet, when the salinity increased to 20‰ and 35‰, the hydrodynamic size of PS-COOH sharply increased to 87 nm and 654 nm after 10 min (**Fig. 7b**) and the aggregation rate increased to 0.041 and 0.948 nm/s (**Table S1**), respectively. Accordingly to the DLVO analysis (**Fig. S5a)**, the energy barrier between PS-COOH was decreased from 29 KT for zero salinity to 15.3, 11.3, 9.0 KT when the salinity was increased to 5‰, 10‰, and 20‰, respectively. The energy barrier dropped below 0 KT when the salinity increased to 35‰. The surface potential of PS-COOH became less negative as the salinity increased due to the charge neutralization and the compression of electrostatic double layer (Li et al., 2020), resulting in weaker electrostatic repulsive forces and faster homoaggregation rates. As a result, the PS-COOH removal efficiency increased from 0 to 3.2% as the salinity increased from 0 to 20‰, and then sharply increased to 84.3% as the salinity increased to 35‰ (**Fig. 7c**). This observation is consistent with previously reported studies. Cai et al. (2018) found that the polystyrene nanoparticles (PS NPs) dispersed well in Milli-Q water with hydrodynamic diameters of ~100 nm at NaCl concentrations ranging from 1 to 50 mmol/L whereas a slight aggregation was observed with 100 mmol/L NaCl. Li et al. (2019) investigated the effects of NaCl on the settling ratios of PS NPs and they found that increasing the NaCl concentration enhanced the settling ratios of PS NPs due to the formation of PS NPs homoaggregates.

With the addition of $AlCl_3$, the zeta potential of PS-COOH changed slowly from -5.3 mV to -8.7, -9.8, -8.6, and -9.9 mV, respectively, as the salinity increased from 0 to 5‰, 10‰, 20‰, and 35‰ (**Fig. 7d**). Correspondingly, the hydrodynamic diameters of PS-COOH changed readily from 1426 nm to 1306, 1394, 1475, and 1577 nm, respectively, after 10 min (**Fig. 7e)**, and the aggregation rates were enhanced from 0.723 to 0.897, 0.803, 0.988, and 1.158 nm/s, respectively (**Table S1**). As described in the DLVO analysis (**Fig. S5b**), the energy barrier between PS-COOH after reaction with $AlCl_3$ with a salinity of 0 was 4.7 KT. Increasing the salinity to 5‰–35‰ decreased the energy barrier to below 0 KT. The increase in salinity resulted in weaker electrostatic repulsive forces, decreased stability, and faster aggregation rates (Drechsler and Grundke 2005). The PS-COOH removal efficiencies with the addition of 10 mg/L $AlCl_3$ at different salinities remained as high as 96% (p value of 0.82 at the 0.05 level of significance).

3.7. Effects of inorganic colloids on PS-COOH removal

Nanoscale Al_2O_3 with a particle size of 20 nm and SiO_2 with a particle size of 50 nm was applied as inorganic colloids in this study. Al_2O_3 was positively charged and SiO_2 was negatively charged in the pH range of 3.0-9.0 (**Fig. S6**). In the absence of $AlCl_3$, the addition of Al_2O_3 led to a sharp increase of zeta potential from -43.6 mV to -5.4 mV due to the charge neutralization (**Fig. 8a**). Correspondingly, the hydrodynamic diameter of PS-COOH was increased to about 250 nm after 10 min (**Fig. 8b**) and the aggregation rate was enhanced to 0.323 nm/s (**Table S1**). The increase of hydrodynamic size was caused by the heteroaggregation between positive charged Al_2O_3 and negative charged PS-COOH (Oriekhova and Stoll, 2018). The addition of SiO_2 slightly changed the zeta potential of PS-COOH from -43.6 mV to -46.1 mV (**Fig. 8a**), and the hydrodynamic diameter of PS-COOH remained constant at 50 nm (**Fig. 8b**) without aggregation (**Table S1**). As a result, the

416 removal efficiency of PS-COOH was increased to 43.3% in the presence of Al_2O_3 and
417 remained at 0 in the presence of SiO_2 (**Fig. 8c**).
418 With the addition of $AlCl_3$, the zeta potential of PS-COOH changed from -3.0 mV to -
419 10.3 mV in the presence of SiO_2 while the zeta potential remained constant at -3.61 mV in
420 the presence of Al_2O_3 (*p* value of 0.97 at the 0.05 level of significance) (**Fig. 8d**).
421 Correspondingly, the hydrodynamic diameter of PS-COOH increased to about 1037 and 1653
422 nm (**Fig. 8e**) and the aggregation rates were 1.114 and 1.308 nm/s, respectively (**Table S1**).
423 The removal efficiencies of PS-COOH after addition of 10 mg/L $AlCl_3$ in the presence and
424 absence of Al_2O_3 and SiO_2 were shown in **Fig. 8f**. In the absence of inorganic colloids, the
425 PS-COOH NPs removal efficiency was 96.6%. The presence of 50 mg/L of SiO_2 decreased
426 the removal efficiency to 93.2% probably due to the fact that the negatively charged SiO_2 can
427 compete with PS-COOH for reacting with $AlCl_3$. Meanwhile, with the addition of $AlCl_3$, the
428 PS-COOH removal efficiency did not show significant difference in the absence and presence
429 of negatively charged Al_2O_3 (*p* value of 1.03 at the 0.05 level of significance).
430
431 *3.8. PS-COOH removal in real surface water*
432 The PS-COOH spiked surface water (PS-COOH = 50 mg/L) contained 15.0 mg/L Cl^-,
433 6.3 mg/L NO_3^-, 30.9 mg/L SO_4^{2-}, 7.8 mg/L K^+, 23.3 mg/L Ca^{2+}, 16.7 mg/L Na^+, 3.4 mg/L
434 Mg^{2+}, and 8.0 mg/L TOC. pH value was measured to be 6.8 and the zeta potential was
435 determined to be -14.9 mV. With the addition of 10 mg/L $AlCl_3$, 90.2% of the PS-COOH
436 was removed while the removal efficiency of the PS-COOH in deionized water was 96.6% (*p*
437 value of 0.016 at the 0.05 level of significance). The decrease in PS-COOH removal
438 efficiency was probably due to the presence of TOC in the surface water. TOC links to the
439 PS-COOH via adsorption or hydrophobic interaction (Hotze et al., 2010), increasing the
440 steric and electrostatic repulsion between the PS-COOH, and thus providing the stabilizing

441 effect. In addition, TOC may compete with PS-COOH for Al, resulting in reduced PS-
442 COOH removal efficiency. After reaction with 10 mg/L $AlCl_3$, TOC in aqueous phase was
443 reduced from 8.0 mg/L to 3.2 mg/L.
444
445 **4. Conclusions**
446 This study comprehensively investigated the removal of nanoplastics from water via
447 coagulation and sedimentation using $AlCl_3$ as a coagulant. PS-COOH NPs appeared as
448 clearly defined and discrete spherical nanoparticles and were well dispersed in water. 10
449 mg/L $AlCl_3$ effectively removed 96.6% of 50 mg/L of PS-COOH after reaction. The added
450 positively charged aluminum ions can compress and even destroy the stable negatively
451 charged PS-COOH surface layer or electron double layer, decreased the stabilizing Coulomb
452 forces between the particles and the energy barrier, and led to higher attachment efficiency
453 and enhanced aggregation rate of PS-COOH. The dominant removal mechanisms include
454 electrostatic adsorption and intermolecular interactions. The PS-COOH removal efficiency
455 increased sharply from 12.0% at pH 3.0 to 96.4% at pH 8.5, and then decreased to 83.7%
456 when pH reached 10.0. Increasing the temperature from 4 to 23 ^{o}C significantly enhanced
457 the PS-COOH removal efficiency from 92.1% to 96.6%. Salinity affects the colloidal
458 stability of the PS-COOH. In the absence of $AlCl_3$, the PS-COOH removal efficiency
459 increased from 0 to 3.2% as the salinity increased from 0 to 20‰, and then sharply increased
460 to 84.3% as the salinity increased to 35‰. With the addition of $AlCl_3$, the PS-COOH
461 removal efficiency remained constant at 96% with the increase of salinity. The addition of
462 negatively charged SiO_2 did not affect the stability of PS-COOH whereas the addition of
463 positively charged Al_2O_3 enhanced the formation of heteroaggregates and sharply increased
464 the PS-COOH removal efficiency from 0 to 43.3%. After the addition of $AlCl_3$, the PS-
465 COOH NPs removal efficiency was 96.6% in the absence and presence of Al_2O_3. Yet, the

presence of SiO_2 decreased the removal efficiency to 93.2%. The addition of 10 mg/L $AlCl_3$ efficiently removed 90.2% of 50 mg/L PS-COOH from real surface water rich in inorganic ions and TOC. This study demonstrated the promise of coagulation and sedimentation using $AlCl_3$ for fast and efficient removal of NPs from natural water bodies. This approach provides an innovative and practical alternative to remove NPs from contaminated aquatic systems.

Acknowledgements

The authors gratefully acknowledge the partial financial supports from Science and Technology Program of Guangzhou (202102010109), Guangdong Basic and Applied Basic Research Foundation (2019A1515012013), Natural Science Foundation of China (42177186), and The Pearl River Talent Program of Guangdong Province (2017GC010331).

References

Andrady, A.L., 2011. Microplastics in the marine environment. Mar. Pollut. Bull. 62(8), 1596-1605.

Auta, H.S., Emenike, C., Fauziah, S., 2017. Distribution and importance of microplastics in the marine environment: a review of the sources, fate, effects, and potential solutions. Environ. Int. 102, 165-176.

Beran, A., Voll, D., Schneider, H., 2001. Dehydration and structural development of mullite precursors: an FTIR spectroscopic study. J. Eur. Ceram. Soc. 21(14), 2479-2485.

Besseling, E., Quik, J.T., Sun, M., Koelmans, A.A., 2017. Fate of nano-and microplastic in freshwater systems: A modeling study. Environ. Pollut. 220, 540-548.

Bottero, J., Tchoubar, D., Cases, J. and Fiessinger, F., 1982. Investigation of the hydrolysis of aqueous solutions of aluminum chloride. 2. Nature and structure by small-angle X-ray scattering. J. Phys. Chem. 86(18), 3667-3673.

Cai, L., Hu, L., Shi, H., Ye, J., Zhang, Y., Kim, H., 2018. Effects of inorganic ions and natural organic matter on the aggregation of nanoplastics. Chemosphere 197, 142-151.

Carr, S.A., Liu, J., Tesoro, A.G., 2016. Transport and fate of microplastic particles in wastewater treatment plants. Water Res. 91, 174-182.

Casado, M.P., Macken, A., Byrne, H.J., 2013. Ecotoxicological assessment of silica and polystyrene nanoparticles assessed by a multitrophic test battery. Environ. Int. 51, 97-105.

Chae, Y., An, Y.-J., 2017. Effects of micro-and nanoplastics on aquatic ecosystems: Current research trends and perspectives. Mar. Pollut. Bull. 124(2), 624-632.

Chen, Y., Tang, X., Shu, J., Wang, X., Hu, W., Shen, Q.D., 2016. Crosslinked P (VDF-CTFE)/PS- COOH nanocomposites for high- energy- density capacitor application. J. Polym. Sci. Pt. B-Polym. Phys. 54(12), 1160-1169.

Costa, T.M., Gallas, M.R., Benvenutti, E.V., da Jornada, J.A., 1999. Study of nanocrystalline γ-Al_2O_3 produced by high-pressure compaction. J. Phys. Chem. B 103(21), 4278-4284.

da Costa, J.P., Santos, P.S.M., Duarte, A.C., Rocha-Santos, T. 2016. (Nano)plastics in the environment – Sources, fates and effects. Sci. Total Environ. 566-567, 15-26.

Derjaguin, B.v., Landau, L., 1993. Theory of the stability of strongly charged lyophobic sols and of the adhesion of strongly charged particles in solutions of electrolytes. Prog. Surf. Sci. 43(1-4), 30-59.

Ding, P., Zhang, J., Song, N., Tang, S., Liu, Y., Shi, L., 2015. Anisotropic thermal conductive properties of hot-pressed polystyrene/graphene composites in the through-plane and in-plane directions. Compos. Sci. Technol. 109, 25-31.

Djebaili, K., Mekhalif, Z., Boumaza, A., Djelloul, A., 2015. XPS, FTIR, EDX, and XRD analysis of Al_2O_3 scales grown on PM2000 alloy. J. Spectrosc. 2015.

do Sul, J.A.I., Costa, M.F., 2014. The present and future of microplastic pollution in the marine environment. Environ. Pollut. 185, 352-364.

Drechsler, A., Grundke, K., 2005. The influence of electrolyte ions on the interaction forces between polystyrene surfaces. Colloid Surf. A-Physicochem. Eng. Asp. 264(1-3), 157-165.

Gigault, J., Hadri, H.E., Nguyen, B., Grassl, B., Rowenczyk, L., Tufenkji, N., Feng, S., Wiesner, M., 2021. Nanoplastics are neither microplastics nor engineered nanoparticles. Nat. Nanotechnol. 16, 501-507.

Gregory, J., Dupont, V., 2001. Properties of flocs produced by water treatment coagulants. Water Sci. Technol. 44(10), 231-236.

Han, W., Bai, Y., Liu, S., Ge, C., Wang, L., Ma, Z., Yang, Y. and Zhang, X., 2017. Enhanced thermal conductivity of commercial polystyrene filled with core-shell structured BN@PS. Compos. Pt. A-Appl. Sci. Manuf. 102, 218-227.

Han, W., Chen, M., Song, W., Ge, C., Zhang, X., 2020. Construction of hexagonal boron nitride@ polystyrene nanocomposite with high thermal conductivity for thermal management application. Ceram. Int. 46(6), 7595-7601.

He, W., Xie, Z., Lu, W., Huang, M., Ma, J., 2019. Comparative analysis on floc growth behaviors during ballasted flocculation by using aluminum sulphate (AS) and polyaluminum chloride (PACl) as coagulants. Sep. Purif. Technol. 213, 176-185.

Hernandez, L.M., Yousefi, N., Tufenkji, N., 2017. Are there nanoplastics in your personal care products? Environ. Sci. Technol. Lett. 4(7), 280-285.

Hotze, E.M., Phenrat, T., Lowry, G.V., 2010. Nanoparticle aggregation: challenges to understanding transport and reactivity in the environment. J. Environ. Qual. 39(6), 1909-1924.

Hu, C., Liu, H., Qu, J., Wang, D., Ru, J., 2006. Coagulation behavior of aluminum salts in eutrophic water: significance of Al13 species and pH control. Environ. Sci. Technol. 40(1), 325-331.

Hu, X., Zhang, Z., Lu, Y., Liu, R., Sun, L., Parkin, I.P., Zhang, X., 2019. One- step synthesis of Ag@PS nanospheres via flash nanoprecipitation. Appl. Organomet. Chem. 33(3), e4713.

Ivleva, N.P., Wiesheu, A.C., Niessner, R., 2017. Microplastic in aquatic ecosystems. Angew. Chem.-Int. Edit. 56(7), 1720-1739.

Izquierdo, P., Feng, J., Esquena, J., Tadros, T.F., Dederen, J.C., Garcia, M.J., Azemar, N., Solans, C., 2005. The influence of surfactant mixing ratio on nano-emulsion formation by the pit method. J. Colloid Interface Sci. 285(1), 388-394.

Lee, D., Condrate, R., Lacourse, W., 2000. FTIR spectral characterization of thin film coatings of oleic acid on glasses Part II Coatings on glass from different media such as water, alcohol, benzene and air. J. Mater. Sci. 35(19), 4961-4970.

Lenz, R., Enders, K., Nielsen, T.G., 2016. Microplastic exposure studies should be environmentally realistic. Proc. Natl. Acad. Sci. U. S. A. 113 (29), E4121-E4122.

Letterman, R., Vanderbrook, S., 1983. Effect of solution chemistry on coagulation with hydrolyzed Al(III): Significance of sulfate ion and pH. Water Res. 17(2), 195-204.

Li, X., He, E., Xia, B., Van Gestel, C.A., Peijnenburg, W.J., Cao, X., Qiu, H., 2020. Impact of CeO_2 nanoparticles on the aggregation kinetics and stability of polystyrene nanoplastics: Importance of surface functionalization and solution chemistry. Water Res., 116324.

Li, Y., Wang, X., Fu, W., Xia, X., Liu, C., Min, J., Zhang, W., Crittenden, J.C., 2019. Interactions between nano/micro plastics and suspended sediment in water: Implications on aggregation and settling. Water Res. 161, 486-495.

Lin, D., Story, S.D., Walker, S.L., Huang, Q., Cai, P., 2016. Influence of extracellular polymeric substances on the aggregation kinetics of TiO_2 nanoparticles. Water Res. 104, 381-388.

Liu, J., Dai, C., Hu, Y., 2018. Aqueous aggregation behavior of citric acid coated magnetite nanoparticles: Effects of pH, cations, anions, and humic acid. Environ. Res. 161, 49-60.

Lu, S., Zhu, K., Song, W., Song, G., Chen, D., Hayat, T., Alharbi, N.S., Chen, C., Sun, Y., 2018. Impact of water chemistry on surface charge and aggregation of polystyrene microspheres suspensions. Sci. Total Environ. 630, 951-959.

Ma, J., Wang, R., Wang, X., Zhang, H., Zhu, B., Lian, L., Lou, D., 2019. Drinking water treatment by stepwise flocculation using polysilicate aluminum magnesium and cationic polyacrylamide. J. Environ. Chem. Eng. 7(3), 103049.

Oriekhova, O., Stoll, S., 2018. Heteroaggregation of nanoplastic particles in the presence of inorganic colloids and natural organic matter. Environ.-Sci. Nano 5(3), 792-799.

Perkins, R.B., Palmer, C.D., 2000. Solubility of $Ca_6[Al(OH)_6]_2(CrO_4)_3 \cdot 26H_2O$, the chromate analog of ettringite; 5–75°C. Appl. Geochem. 15(8), 1203-1218.

Petosa, A.R., Jaisi, D.P., Quevedo, I.R., Elimelech, M., Tufenkji, N., 2010. Aggregation and deposition of engineered nanomaterials in aquatic environments: role of physicochemical interactions. Environ. Sci. Technol. 44(17), 6532-6549.

583 Qiu, F., Lv, H., Zhao, X., Zhao, D., 2019. Impact of an Extreme Winter Storm Event on the
584 Coagulation/Flocculation Processes in a Prototype Surface Water Treatment Plant:
585 Causes and Mitigating Measures. Int. J. Environ. Res. Public Health 16(15), 2808.

586 Rajala, K., Grönfors, O., Hesampour, M., Mikola, A., 2020. Removal of microplastics from
587 secondary wastewater treatment plant effluent by coagulation/flocculation with iron,
588 aluminum and polyamine-based chemicals. Water Res. 183, 116045.

589 Saliu, F., Montano, S., Garavaglia, M.G., Lasagni, M., Seveso, D., Galli, P., 2018.
590 Microplastic and charred microplastic in the Faafu Atoll, Maldives. Mar. Pollut. Bull.
591 136, 464-471.

592 Sennato, S., Truzzolillo, D., Bordi, F., Sciortino, F., Cametti, C., 2009. Colloidal particle
593 aggregates induced by particle surface charge heterogeneity. Colloid Surf. A-
594 Physicochem. Eng. Asp. 343(1-3), 34-42.

595 Singh, N., Tiwari, E., Khandelwal, N., Darbha, G.K., 2019. Understanding the stability of
596 nanoplastics in aqueous environments: effect of ionic strength, temperature, dissolved
597 organic matter, clay, and heavy metals. Environ.-Sci. Nano 6(10), 2968-2976.

598 Skaf, D.W., Punzi, V.L., Rolle, J.T., Kleinberg, K.A., 2020. Removal of micron-sized
599 microplastic particles from simulated drinking water via alum coagulation. Chem. Eng.
600 J. 386, 123807.

601 Song, Y.K., Hong, S.H., Jang, M., Han, G.M., Jung, S.W., Shim, W.J., 2017. Combined
602 effects of UV exposure duration and mechanical abrasion on microplastic fragmentation
603 by polymer type. Environ. Sci. Technol. 51(8), 4368-4376.

604 Talvitie, J., Mikola, A., Koistinen, A., Setälä, O., 2017. Solutions to microplastic pollution–
605 Removal of microplastics from wastewater effluent with advanced wastewater treatment
606 technologies. Water Res. 123, 401-407.

607 Vangara, R., Brown, D., van Swol, F., Petsev, D., 2017. Electrolyte solution structure and its
608 effect on the properties of electric double layers with surface charge regulation. J.
609 Colloid Interface Sci. 488, 180-189.

610 Wang, J., Zhao, X., Wu, A., Tang, Z., Niu, L., Wu, F., Wang, F., Zhao, T., Fu, Z., 2020.
611 Aggregation and stability of sulfate-modified polystyrene nanoplastics in synthetic and
612 natural waters. Environ. Pollut., 114240.

613 Wong, K., Mukherjee, B., Kahler, A.M., Zepp, R., Molina, M., 2012. Influence of inorganic
614 ions on aggregation and adsorption behaviors of human adenovirus. Environ. Sci.
615 Technol. 46(20), 11145-11153.

616 Wu, J., Jiang, R., Lin, W., Ouyang, G., 2019. Effect of salinity and humic acid on the
617 aggregation and toxicity of polystyrene nanoplastics with different functional groups and
618 charges. Environ. Pollut. 245, 836-843.

619 Wu, X., Ge, X., Wang, D., Tang, H., 2007. Distinct coagulation mechanism and model
620 between alum and high Al13-PACl. Colloid Surf. A-Physicochem. Eng. Asp. 305(1-3),
621 89-96.

622 Wu, X., Liu, P., Huang, H., Gao, S., 2020. Adsorption of triclosan onto different aged
623 polypropylene microplastics: Critical effect of cations. Sci. Total Environ. 717, 137033.

624 Yang, D., Shi, H., Li, L., Li, J., Jabeen, K., Kolandhasamy, P., 2015. Microplastic pollution
625 in table salts from China. Environ. Sci. Technol. 49(22), 13622-13627.

626 Yang, Z.L., Gao, B.Y., Yue, Q.Y., Wang, Y., 2010. Effect of pH on the coagulation
627 performance of Al-based coagulants and residual aluminum speciation during the
628 treatment of humic acid–kaolin synthetic water. J. Hazard. Mater. 178(1-3), 596-603.

629 You, Z., Zhuang, C., Sun, Y., Zhang, S., Zheng, H., 2019. Efficient Removal of TiO_2
630 Nanoparticles by Enhanced Flocculation–Coagulation. Ind. Eng. Chem. Res. 58(31),
631 14528-14537.

632 Yuan, H., Wang, Y., Li, T., Wang, Y., Ma, P., Zhang, H., Yang, W., Chen, M., Dong, W.,
633 2019. Fabrication of thermally conductive and electrically insulating polymer
634 composites with isotropic thermal conductivity by constructing a three-dimensional
635 interconnected network. Nanoscale 11(23), 11360-11368.

636 Zhang, P., Wu, Z., Zhang, G., Zeng, G., Zhang, H., Li, J., Song, X., Dong, J., 2008.
637 Coagulation characteristics of polyaluminum chlorides PAC-Al30 on humic acid
638 removal from water. Sep. Purif. Technol. 63(3), 642-647.

639 Zhou, G., Wang, Q., Li, J., Li, Q., Xu, H., Ye, Q., Wang, Y., Shu, S., Zhang, J. 2021. Removal
640 of Removal of polystyrene and polyethylene microplastics using PAC and
641 FeCl3 coagulation: Performance and mechanism. Sci. Total Environ. 752, 141837.

Figure

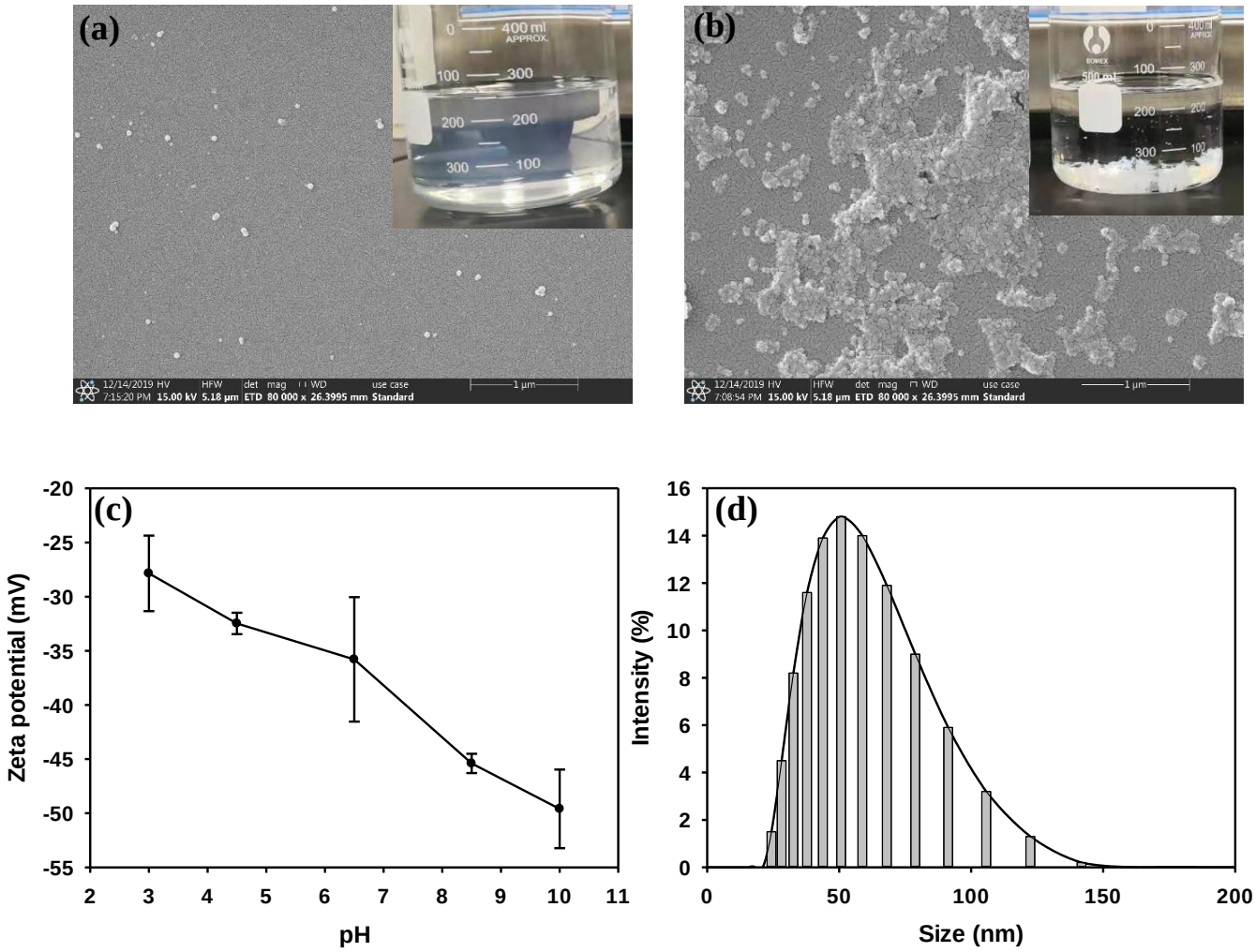

Fig. 1. Digital photographs and SEM images of (a) PS-COOH and (b) PS-COOH flocs after coagulation, (c) zeta potentials of PS-COOH as a function of pH, and (d) size distribution histograms of PS-COOH.

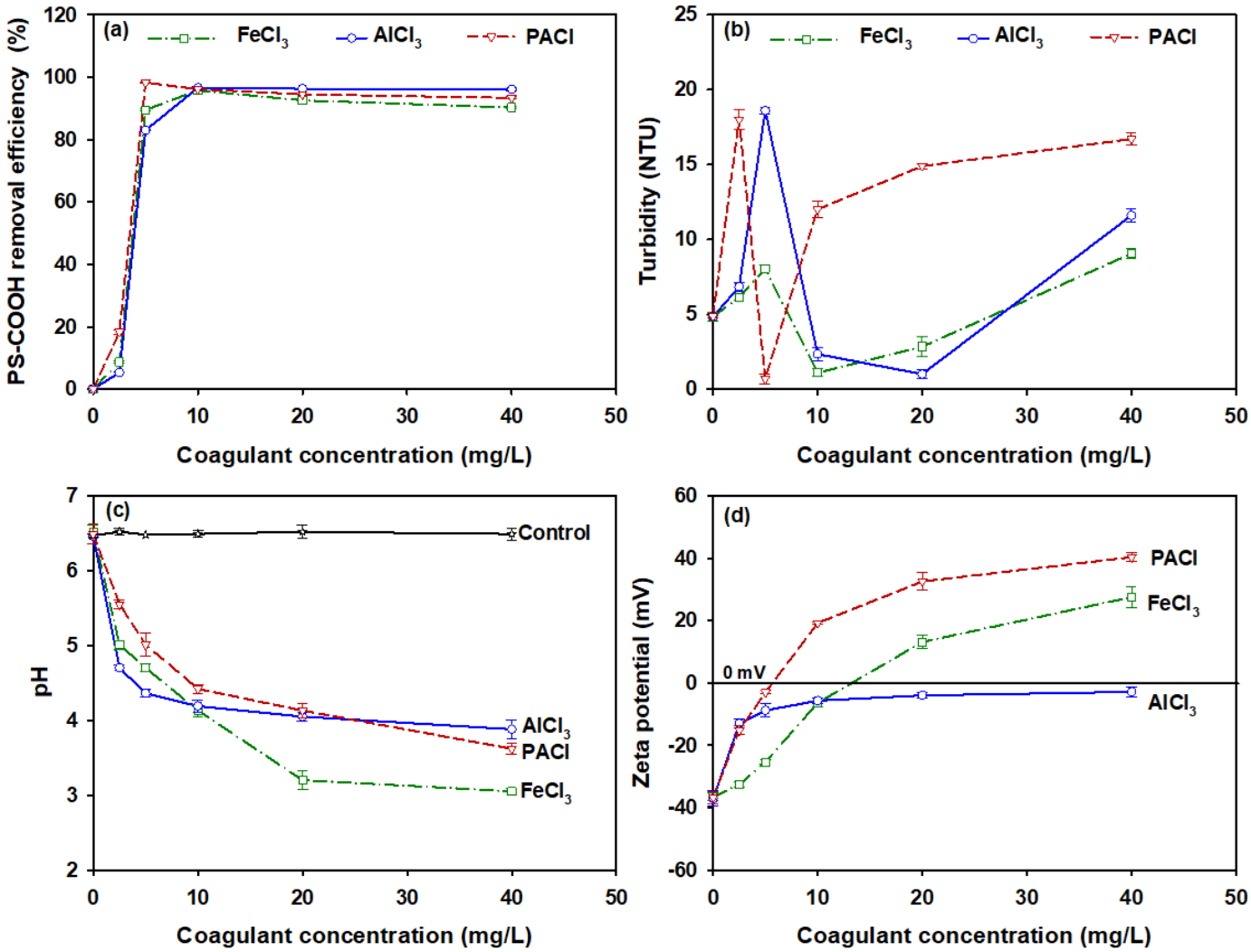

Fig. 2. Effects of different coagulant and coagulant dosage on (a) PS-COOH removal efficiency, (b) residual turbidity, (c) pH and (d) zeta potential of PS-COOH suspensions before and after coagulation with different types and concentrations of coagulants. Experimental conditions: Initial concentration of PS-COOH = 50 mg/L, $AlCl_3$, $FeCl_3$, and PACl concentration = 2.5, 5, 8, 10, 20, and 40 mg/L, initial pH = 6.5, and reaction volume = 300 mL. Data plotted as mean of duplicates and error bars (calculated as standard deviation) indicate data reproducibility.

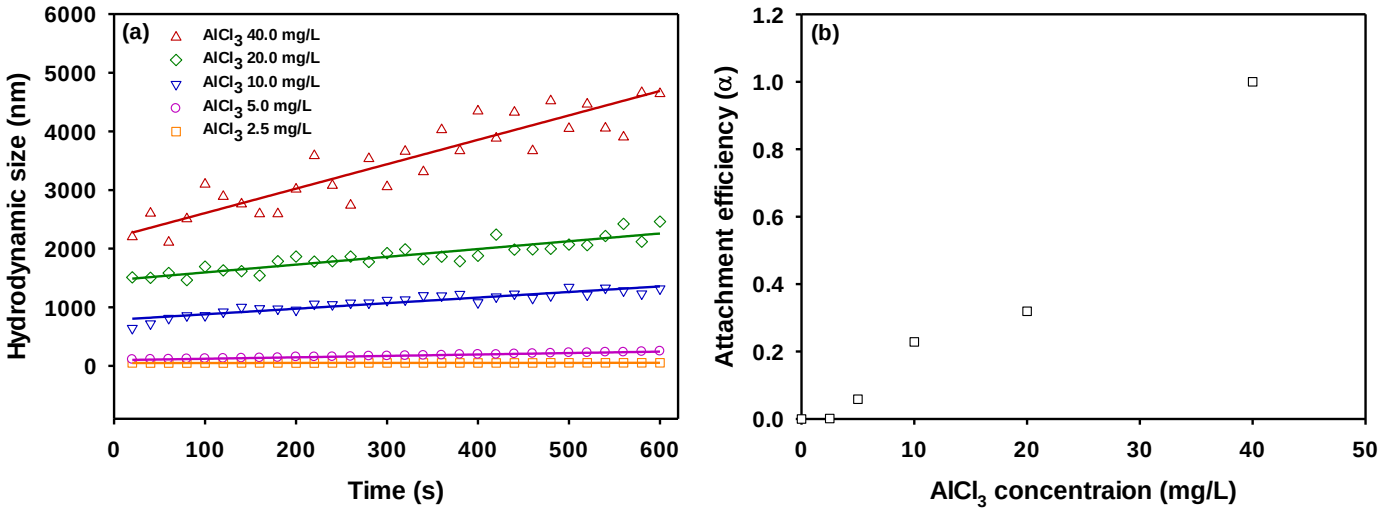

Fig. 3. (a) Change of hydrodynamic size over time for PS-COOH after mixing with $AlCl_3$ of different concentrations. The straight lines indicate linear fit in order to obtain the aggregation rate. (b) Attachment efficiency of PS-COOH as a function of $AlCl_3$ concentration.

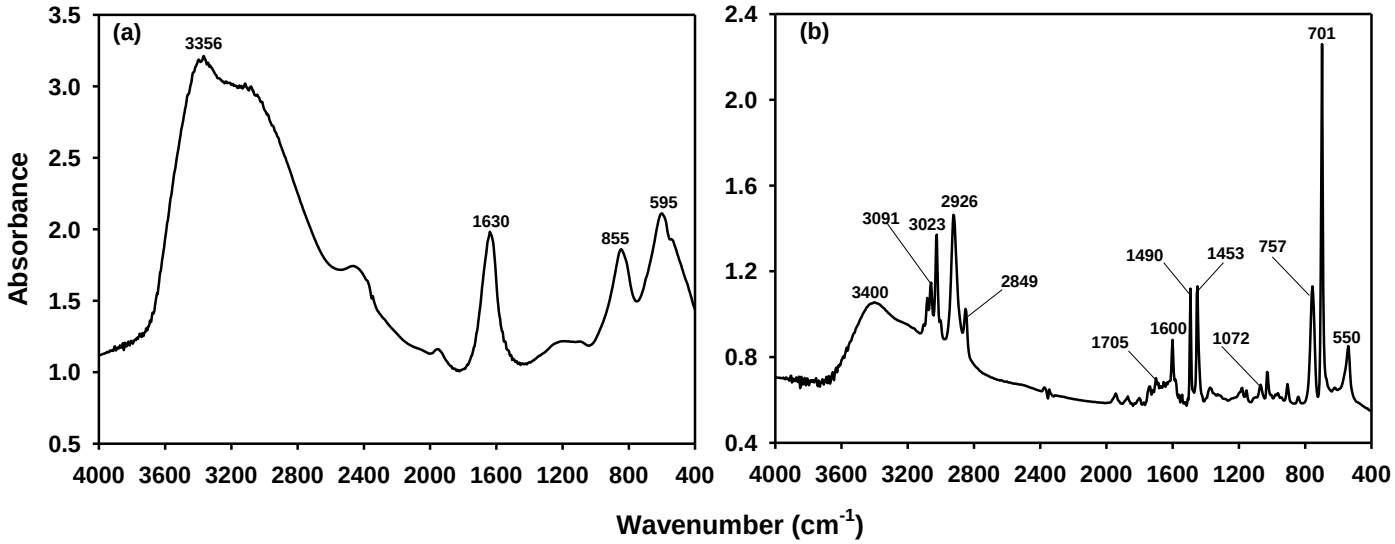

Fig. 4. FTIR spectra of (a) $AlCl_3 \cdot 6H_2O$ and (b) flocs of PS-COOH after coagulation. Experimental conditions: initial PS-COOH concentration = 50 mg/L, $AlCl_3$ concentration = 10 mg/L, and reaction volume = 300 mL. The flocs of PS-COOH after coagulation were collected and vacuum-dried in a freeze drier.

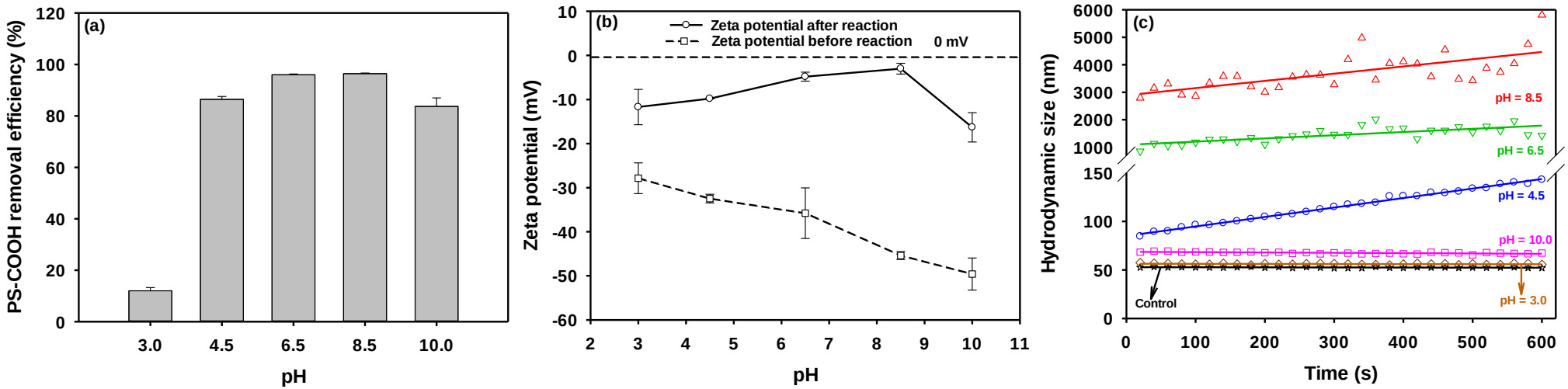

Fig. 5. (a) Effects of pH on PS-COOH removal efficiency, (b) zeta potentials of PS-COOH before and after mixing with $AlCl_3$ at different pH, and (c) change of hydrodynamic size over time for PS-COOH after mixing with $AlCl_3$ at different pH. Experimental conditions: Initial concentration of PS-COOH = 50 mg/L, initial pH = 3.0, 4.5, 6.5, 8.5, and 10.0, $AlCl_3$ concentration = 10 mg/L, and reaction volume = 300 mL. Data plotted as mean of duplicates and error bars (calculated as standard deviation) indicate data reproducibility.

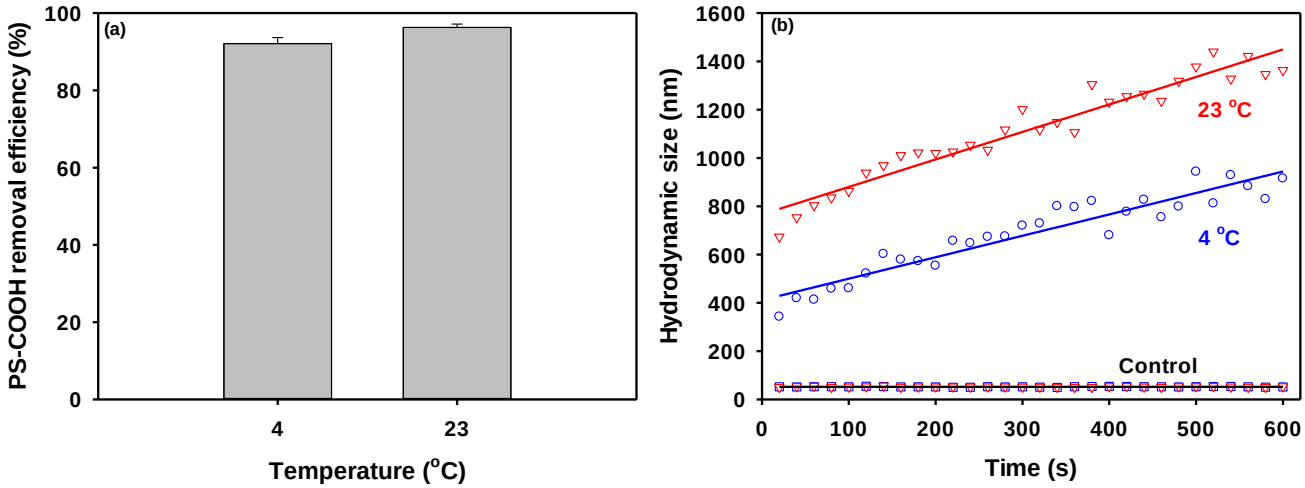

Fig. 6. (a) Effects of temperature on PS-COOH removal efficiency and (b) change of hydrodynamic size over time for PS-COOH before and after mixing with $AlCl_3$ at different temperature. Experimental conditions: Initial concentration of PS-COOH = 50 mg/L, $AlCl_3$ concentration = 10 mg/L, temperature = 4 and 23 °C, initial pH = 6.5, and reaction volume = 300 mL. Data plotted as mean of duplicates and error bars (calculated as standard deviation) indicate data reproducibility.

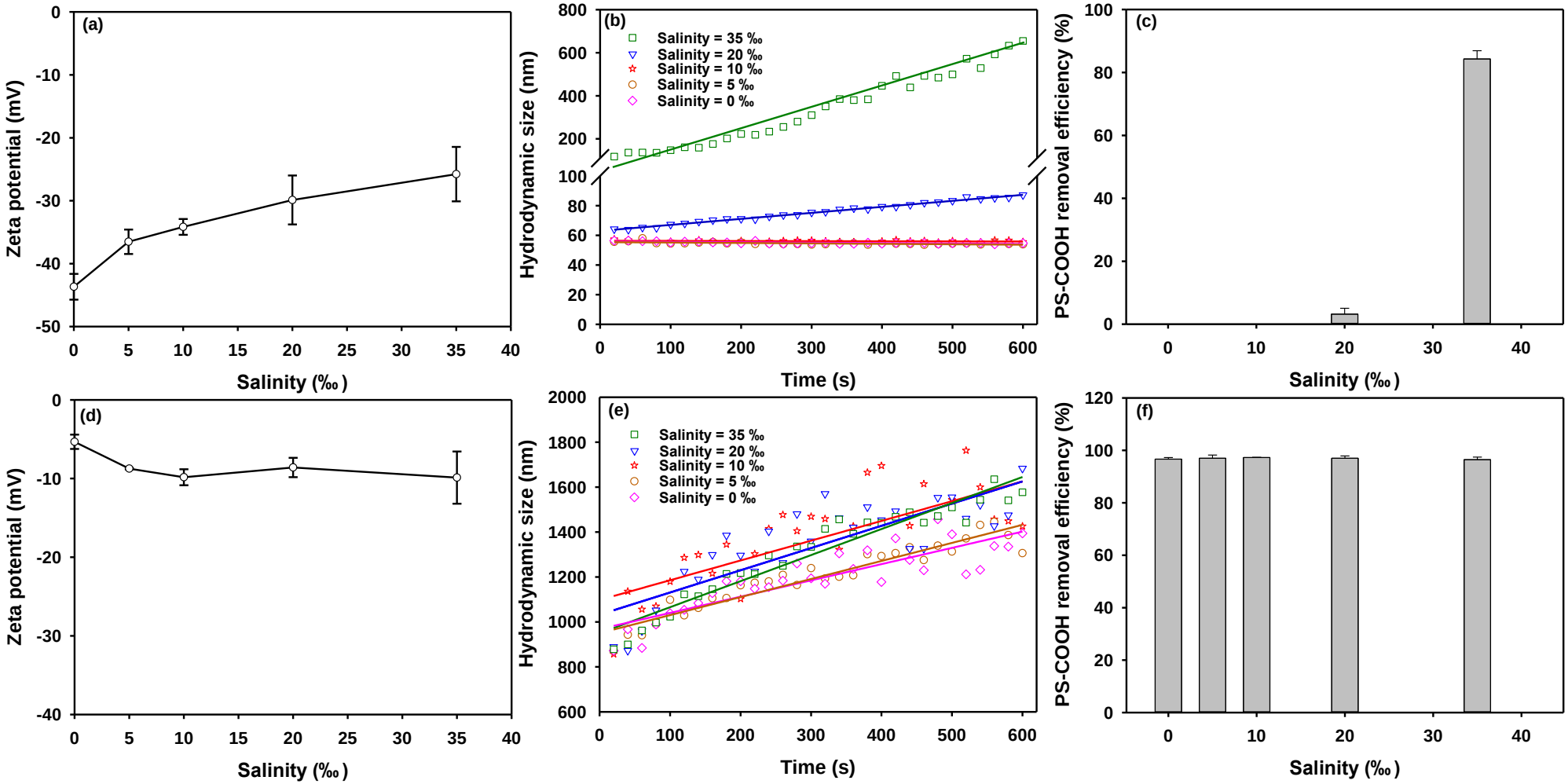

Fig. 7. Zeta potentials of PS-COOH with different salinities (a) in the absence and (d) in the presence of $AlCl_3$; change of hydrodynamic diameter over time for PS-COOH at different salinities (b) in the absence and (e) in the presence of $AlCl_3$; effects of salinity on the PS-COOH removal efficiency (c) in the absence and (f) in the presence of $AlCl_3$. Experimental conditions: Initial concentration of PS-COOH = 50 mg/L, salinity = 5, 10, 20, and 35‰, $AlCl_3$ concentration = 10 mg/L, initial pH = 6.5, and reaction volume = 300 mL. Data plotted as mean of duplicates and error bars indicate data reproducibility.

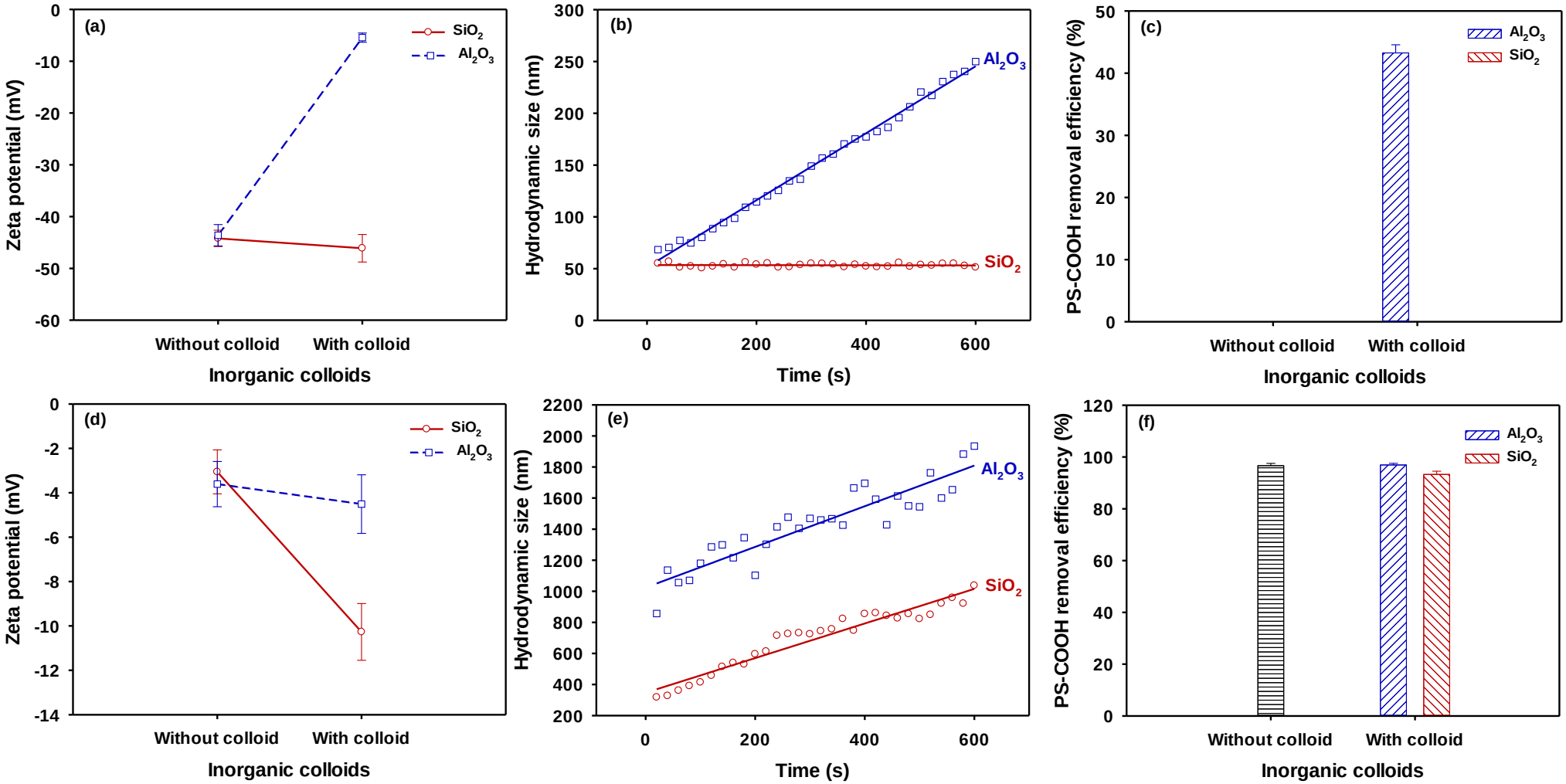

Fig. 8. Zeta potentials of PS-COOH with and without colloids (a) in the absence and (d) in the presence of $AlCl_3$; change of hydrodynamic diameter over time for PS-COOH with and without colloids (b) in the absence and (e) in the presence of $AlCl_3$; effects of inorganic colloids on the PS-COOH removal efficiency (c) in the absence and (f) in the presence of $AlCl_3$. Experimental conditions: Initial concentration of PS-COOH = 50 mg/L, Al_2O_3 concentration = 30 mg/L, SiO_2 concentration = 50 mg/L, $AlCl_3$ concentration = 10 mg/L, initial pH = 6.5, and reaction volume = 300 mL. Data plotted as mean of duplicates and error bars (calculated as standard deviation) indicate data reproducibility.